

## Microscopic theory of second-order Raman scattering in silicon under uniaxial stress

C. H. Grein, S. Zollner, and M. Cardona

*Max Planck Institut für Festkörperforschung, Heisenbergstrasse 1, D-7000 Stuttgart 80,  
Federal Republic of Germany*

(Received 9 October 1990)

A microscopic calculation of the second-order Raman-scattering efficiency of silicon, with special emphasis on the effects of uniaxial stress, is presented. Employing diagrammatic perturbation theory, the scattering efficiency is obtained for incident- and scattered-photon energies either on or off resonance. A numerical evaluation employs realistic models for the electronic band structure and phonon spectra, and sums over all two-, three-, and four-band scattering channels. The scattering efficiency is normalized by the integrated first-order efficiency, and the results of the calculation are quantitatively compared with experimental data for second-order Raman scattering in crystalline silicon under [001] stress, taken with an incident laser energy of 2.34 eV.

### I. INTRODUCTION

Raman scattering of light is one of the most powerful methods for studying various types of elementary excitations in solids.<sup>1</sup> Here we consider vibrational Raman scattering which involves inelastic light scattering by a crystal due to the modulation of the crystal polarizability by phonons. A great deal of theoretical effort has been invested in the development of a description of the scattering processes.<sup>1-7</sup> Microscopic calculations employ perturbation theory to formulate expressions for the scattering cross section; however, the complexity of these expressions, especially for higher-order scattering, makes their evaluation difficult.<sup>6</sup> Thus, for physical insight and for comparison with experiment, phenomenological theories have often been employed. These theories involve the expansion of the dielectric function as a function of phonon coordinates. The scattered light intensity for a given number of phonon absorptions and/or emissions is then obtained from the corresponding term in the expansion. These terms are often treated as parameters adjusted to fit experimental data,<sup>8,9</sup> rather than being obtained from the microscopic evaluation of the derivatives of the dielectric function.

Here we derive a microscopic theory and present the results of the calculation of the second-order Raman spectra of crystalline Si under uniaxial stress. In contrast with earlier calculations of resonant (i.e., the laser or scattered frequency is near an optically strong interband transition) spectra, our results are valid for photon frequencies either on or off resonance. We employ realistic models for the electronic band structure and the phonon spectra, and sum over all possible scattering channels (up to four-band terms); these are also improvements over most earlier approaches. As a consequence of the large number of scattering channels and the need to perform two nested Brillouin-zone sums (one for the wave vector of the electron or hole, the other for the wave vector of one of the involved phonons), the numerical calculations

are rather lengthy. Our work serves as a generalization of an earlier calculation of the resonant second-order Raman spectra of unstrained semiconductors.<sup>10</sup>

A number of experiments have examined the effects of uniaxial stress on resonant Raman spectra.<sup>11-13</sup> Recent data for uniaxially stressed silicon with which our calculations are compared were obtained off resonance<sup>14</sup> with an incident laser energy of 2.34 eV. Off-resonance measurements probe deeper into the sample than on-resonance measurements, and therefore are less affected by surface effects. For example, the surface strain may be different from the strain in the bulk. The consideration of the effects of uniaxial stress also stems from recent interest in strained layer Si/Ge superlattices.<sup>15,16</sup>

In Sec. II expressions are obtained for the second-order Raman-scattering efficiency and its normalization with respect to the integrated first-order efficiency. Section III discusses the methods employed to numerically evaluate these expressions. A comparison with experimental data for Si takes place in Sec. IV, and conclusions are drawn in Sec. V.

### II. THEORY

The microscopic theory of Raman scattering was first formulated by Born and Huang<sup>2</sup> and Loudon,<sup>5</sup> and formalized by Gauguly and Birman.<sup>6</sup> Our calculation is most similar to that of Klein<sup>17</sup> who obtained expressions for the second-order Raman-scattering efficiency in transition metals and compounds through an application of the theory of Kawabata.<sup>7</sup> Here, we have tailored Kawabata's theory towards applicability in semiconductors.

The scattering probability per unit path length, per unit scattering frequency, and per unit solid angle (the scattering efficiency) for second-order scattering is given by<sup>17,18</sup>

$$\frac{\partial^2 S}{\partial \Omega \partial \omega_R} = \left( \frac{\omega_s}{c} \right)^4 \sum_{\alpha, \beta, \gamma, \delta} I_{\alpha\beta\gamma\delta}^{(2)} \hat{e}_{L\alpha} \hat{e}_{L\gamma}^* \hat{e}_{S\beta} \hat{e}_{S\delta}^*, \quad (2.1)$$

where  $\omega_R$  (the Raman shift) is the difference between the incident  $\omega_L$  and scattered  $\omega_S$  frequencies,  $c$  is the speed of light in vacuum, and  $\hat{e}_{L,S}$  are the photon polarization vectors for incident and scattered light. The tensor  $I_{\alpha\beta\gamma\delta}^{(2)}$  for second-order Stokes-Stokes scattering in the one-electron approximation may be expressed in terms of the second-order Raman tensor  $a_{\alpha\beta}^{(2)}$  as

$$I_{\alpha\beta\gamma\delta}^{(2)} = \frac{1}{N} \sum_{\mathbf{Q}, j, j'} a_{\alpha\beta}^{(2)*}(\mathbf{Q}j) a_{\gamma\delta}^{(2)}(\mathbf{Q}j') \delta(\omega_R - \omega_{\mathbf{Q}j} - \omega_{\mathbf{Q}j'}) \times [n(\omega_{\mathbf{Q}j}) + 1][n(\omega_{\mathbf{Q}j'}) + 1], \quad (2.2)$$

where  $N$  is the number of primitive cells in the sample,  $\mathbf{Q}$  is the wave vector of one of the phonons (momentum conservation requires that the other phonon has momentum  $-\mathbf{Q}$ ),  $j$  is the phonon branch index, and

$$n(\omega_{\mathbf{Q}j}) = [\exp(\hbar\omega_{\mathbf{Q}j}/k_B T) - 1]^{-1}$$

is the Bose function. In tetrahedral semiconductors the Stokes-anti-Stokes contributions (difference processes) are weak in the spectral range of interest, and may be neglected.

The contributions to the second-order Raman tensor are most easily found with the aid of Feynman diagrams (Fig. 1). Figures 1(a) and 1(b) describe the hole or electron emitting two phonons with an interaction vertex determined by the intrinsic electron-two-phonon interaction. Figures 1(c)–1(e) describe the phonon emissions through the electron-one-phonon interaction taken to second order. Figures 1(f)–1(i) describe iterated first-order events with an intermediate state consisting of a virtual photon. The diagrams may be grouped into resonant and nonresonant types; the (non)resonant diagrams are characterized by the scattered photon being emitted (before) after the incident photon is absorbed. It would be a tedious task to evaluate all the diagrams in Fig. 1; fortunately many can be shown to be negligible. The diagrams corresponding to iterated first-order events [1(f)–1(i)] have a scattering efficiency comparable to the first-order scattering efficiency squared and thus may be neglected. We find that for purposes of comparing with the experimental data for Si obtained with  $\hbar\omega_L = 2.34$  eV (see Sec. IV), the contributions of the nonresonant terms may be neglected. For lower  $\omega_L$ 's the contributions of the nonresonant terms will become significant. For the case of resonant Raman scattering considered in Ref. 10, four diagrams [Fig. 1(a)–1(d)] dominate the scattering. For the more general off-resonance case considered here 42 diagrams give significant contributions and thus need to be taken into account, neglecting the nonresonant and iterated first-order diagrams.

The diagrams were evaluated using Matsubara thermal Green's functions.<sup>19</sup> We illustrate the technique by calculating the contribution of Fig. 1(d) to the Raman tensor. The following complex boson frequencies are inserted into the electron loop: at the incident photon vertex,  $i\omega_0$  which will later be analytically continued to  $\omega_L + i\eta$ ; at the first phonon vertex,  $i\omega_p$  which will be analytically continued to  $\omega_{\mathbf{Q}j}$ ; at the second phonon vertex,  $i\omega_{p'}$  which will be analytically continued to  $\omega_{-\mathbf{Q}j'} = \omega_{\mathbf{Q}j'}$ ; and

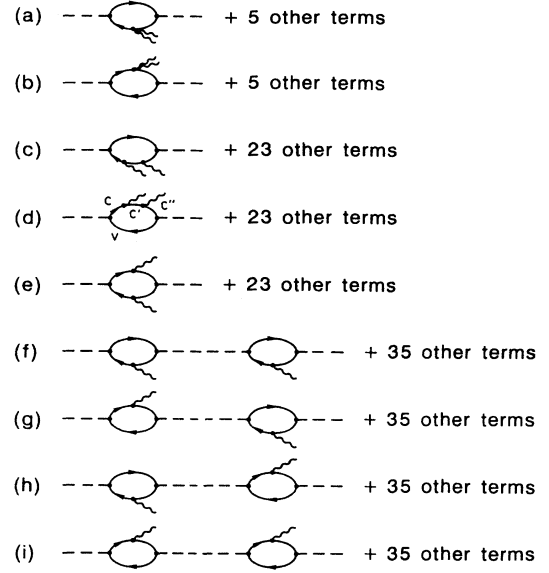


FIG. 1. Feynman diagrams describing processes contributing to second-order Raman scattering. The incident photon (left dashed line) creates a virtual electron-hole pair (solid loop). The electron and/or hole may emit phonons (wavy lines) before the electron-hole pair recombines and emits the scattered photon. In (f)–(i), there exists an intermediate state consisting of a virtual photon. The other terms which are not drawn are obtained by permuting the vertices of the drawn diagrams.

at the scattered photon vertex  $i\omega_r$ , which will be analytically continued to  $\omega_s$ . Each frequency is an integral multiple of  $2\pi/\beta$ , where  $\beta = 1/k_B T$ . Then the contribution of the fermion propagators in diagram 1(d) is

$$\frac{2}{\beta} \sum_{\mathbf{k}, v, c, c''} M \sum_{i\omega_n} G^0(\mathbf{k}v, i\omega_n) G^0(\mathbf{k}c, i\omega_n + i\omega_0) \times G^0(\mathbf{k} + \mathbf{Q}c', i\omega_n + i\omega_0 - i\omega_p) \times G^0(\mathbf{k}c'', i\omega_n + i\omega_0 - i\omega_p - i\omega_{p'}), \quad (2.3a)$$

where  $M$  denotes the matrix elements

$$M = \langle \mathbf{k}v | H_{e-r} | \mathbf{k}c \rangle \langle \mathbf{k}c | H_{e-p} | \mathbf{k} + \mathbf{Q}c' \rangle \times \langle \mathbf{k} + \mathbf{Q}c' | H_{e-p} | \mathbf{k}c'' \rangle \langle \mathbf{k}c'' | H_{e-r} | \mathbf{k}v \rangle, \quad (2.3b)$$

the fermion Matsubara Green's function is

$$G^0(\mathbf{k}m, i\omega_n) = \frac{1}{i\omega_n - \epsilon_{\mathbf{k}m}}, \quad (2.3c)$$

$\epsilon_{\mathbf{k}m}$  denotes the energy of electronic state  $m$  with momentum  $\mathbf{k}$  relative to the Fermi energy,  $H_{e-r}$  is the electron-photon interaction vertex, and  $H_{e-ph}$  is the electron-one-phonon interaction vertex. Evaluating the frequency summation gives

$$2 \sum_{\mathbf{k}, v, c, c'} M \left[ \frac{f(\epsilon_{\mathbf{k}v})}{(\epsilon_{\mathbf{k}v} + i\omega_0 - \epsilon_{\mathbf{k}c})(\epsilon_{\mathbf{k}v} + i\omega_0 - i\omega_p - \epsilon_{\mathbf{k}+Qc})(\epsilon_{\mathbf{k}v} + i\omega_0 - i\omega_p - i\omega_{p'} - \epsilon_{\mathbf{k}c''})} + \frac{f(\epsilon_{\mathbf{k}c})}{(\epsilon_{\mathbf{k}c} - i\omega_0 - \epsilon_{\mathbf{k}v})(\epsilon_{\mathbf{k}c} - i\omega_p - \epsilon_{\mathbf{k}+Qc})(\epsilon_{\mathbf{k}c} - i\omega_p - i\omega_{p'} - \epsilon_{\mathbf{k}c''})} + \frac{f(\epsilon_{\mathbf{k}+Qc'})}{(\epsilon_{\mathbf{k}+Qc'} - i\omega_0 + i\omega_p - \epsilon_{\mathbf{k}c})(\epsilon_{\mathbf{k}+Qc'} + i\omega_p - \epsilon_{\mathbf{k}c})(\epsilon_{\mathbf{k}+Qc'} - i\omega_{p'} - \epsilon_{\mathbf{k}c})} + \frac{f(\epsilon_{\mathbf{k}c''})}{(\epsilon_{\mathbf{k}c''} - i\omega_0 + i\omega_p + i\omega_{p'} - \epsilon_{\mathbf{k}v})(\epsilon_{\mathbf{k}c''} + i\omega_p + i\omega_{p'} - \epsilon_{\mathbf{k}c})(\epsilon_{\mathbf{k}c''} + i\omega_{p'} - \epsilon_{\mathbf{k}+Qc'})} \right], \quad (2.4)$$

where the Fermi function is  $f(\epsilon) = 1/(e^{\beta\epsilon} + 1)$ , and the zero of the energy scale was chosen to be the Fermi energy. Our calculation differs from that for metals<sup>7,17</sup> since the gap in nondegenerate semiconductors implies that it is a good approximation to assume that in the initial state all valence-band states are occupied and all conduction-band states are unoccupied. Then the final three terms in (2.4) can be neglected. Employing the  $H_{e-r}$  and  $H_{e-ph}$  of Ref. 20, treating the boson propagators as in Refs. 7 and 17, and performing the analytic continuations on the boson frequencies gives the contribution of diagram 1(d) to the Raman tensor as given below.

The contributions of the most resonant terms of each of the three types (hole emitting two phonons, electron emitting two phonons, and electron and hole each emitting a phonon) are given in the following expression for the Raman tensor. For brevity the other terms are not written here although they are included in the calculation described in the following sections. The second-order Raman tensor may be written as

$$a_{\alpha\beta}^{(2)}(\mathbf{Q}j j') = \frac{2}{N} \sum_{\mathbf{k}, v, v', c, c'} \{ \chi_{\alpha\beta}(\mathbf{k}v, \mathbf{k}c, \mathbf{k}v', \mathbf{k}c') [ \delta_{c,c'} \Delta_{\mathbf{Q}j j'}^{(2)}(\mathbf{k}v, \mathbf{k}v', \mathbf{k}c) + \delta_{v,v'} \Delta_{\mathbf{Q}j j'}^{(2)}(\mathbf{k}c', \mathbf{k}c, \mathbf{k}v) ] - \chi_{\alpha\beta}(\mathbf{k}v, \mathbf{k}c, \mathbf{k}+Qv', \mathbf{k}+Qc') \Delta_{\mathbf{Q}j j'}^{(1;1)}(\mathbf{k}c, \mathbf{k}c', \mathbf{k}v, \mathbf{k}v') \} + \dots \quad (2.5a)$$

where the ellipsis represents 37 other terms, and where

$$\Delta_{\mathbf{Q}j j'}^{(2)}(\mathbf{k}v, \mathbf{k}v', \mathbf{k}c) = \sum_{\kappa, \kappa', m} \left[ \left( \frac{\hbar^2}{4M_{\kappa} M_{\kappa'} \omega_{\mathbf{Q}j} \omega_{\mathbf{Q}j'}} \right)^{1/2} e_{\mu}^*(\mathbf{Q}, j, \kappa) e_{\nu}(\mathbf{Q}, j', \kappa') e^{i\mathbf{Q} \cdot (\tau_{\kappa'} - \tau_{\kappa})} \times \left[ \frac{\langle \mathbf{k}v | \partial V / \partial R_{\mu}(\kappa) | \mathbf{k}+Qm \rangle \langle \mathbf{k}+Qm | \partial V / \partial R_{\nu}(\kappa') | \mathbf{k}v' \rangle}{(\hbar\omega_L - \epsilon_{\mathbf{k}c} + \epsilon_{\mathbf{k}+Qm} + \hbar\omega_{\mathbf{Q}j} + i\eta)(\hbar\omega_L - \epsilon_{\mathbf{k}c} + \epsilon_{\mathbf{k}v} + i\eta)(\hbar\omega_L - \epsilon_{\mathbf{k}c} + \epsilon_{\mathbf{k}v'} - \hbar\omega_{\mathbf{Q}j} - \hbar\omega_{\mathbf{Q}j'} + i\eta)} - \left[ \frac{\hbar e_{\mu}^*(\mathbf{Q}, j, \kappa) e_{\nu}(\mathbf{Q}, j', \kappa)}{4M_{\kappa} \omega_{\mathbf{Q}j}^{1/2} \omega_{\mathbf{Q}j'}^{1/2}} + \frac{\hbar e_{\mu}^*(\mathbf{Q}, j, \kappa') e_{\nu}(\mathbf{Q}, j', \kappa')}{4M_{\kappa'} \omega_{\mathbf{Q}j}^{1/2} \omega_{\mathbf{Q}j'}^{1/2}} \right] \right] \times \left[ \frac{\langle \mathbf{k}v | \partial V / \partial R_{\mu}(\kappa) | \mathbf{k}m \rangle \langle \mathbf{k}m | \partial V / \partial R_{\nu}(\kappa') | \mathbf{k}v' \rangle}{(\hbar\omega_L - \epsilon_{\mathbf{k}c} + \epsilon_{\mathbf{k}m} + i\eta)(\hbar\omega_L - \epsilon_{\mathbf{k}c} + \epsilon_{\mathbf{k}v} + i\eta)(\hbar\omega_L - \epsilon_{\mathbf{k}c} + \epsilon_{\mathbf{k}v'} + i\eta)} \right] \quad (2.5b)$$

corresponds to the hole-emitting two phonons (and is closely related to the electron-two-phonon deformation potential, see Ref. 10);  $\Delta_{\mathbf{Q}j j'}^{(2)}(\mathbf{k}c', \mathbf{k}c, \mathbf{k}v)$  (corresponding to the electron-emitting two phonons) is the same as (2.5b) with the replacements  $v \rightarrow c'$ ,  $v' \rightarrow c$ ,  $c \rightarrow v$ , except for the replacement of the first-energy denominator in the first term with  $(\hbar\omega_L + \epsilon_{\mathbf{k}v} - \epsilon_{\mathbf{k}+Qm} - \hbar\omega_{\mathbf{Q}j})$  and the replacement of the first-energy denominator in the second term with  $(\hbar\omega_L + \epsilon_{\mathbf{k}v} - \epsilon_{\mathbf{k}m})$ :

$$\Delta_{\mathbf{Q}j j'}^{(1;1)}(\mathbf{k}c, \mathbf{k}c', \mathbf{k}v, \mathbf{k}v') = \sum_{\kappa, \kappa'} \left[ \left( \frac{\hbar^2}{4M_{\kappa} M_{\kappa'} \omega_{\mathbf{Q}j} \omega_{\mathbf{Q}j'}} \right)^{1/2} e_{\mu}^*(\mathbf{Q}, j, \kappa') e_{\nu}(\mathbf{Q}, j', \kappa) e^{i\mathbf{Q} \cdot (\tau_{\kappa} - \tau_{\kappa'})} \times \left[ \frac{\langle \mathbf{k}v | \partial V / \partial R_{\mu}(\kappa) | \mathbf{k}+Qv' \rangle \langle \mathbf{k}+Qc' | \partial V / \partial R_{\nu}(\kappa') | \mathbf{k}c \rangle}{(\hbar\omega_L - \epsilon_{\mathbf{k}c} + \epsilon_{\mathbf{k}+Qv'} + \hbar\omega_{\mathbf{Q}j} + i\eta)(\hbar\omega_L - \epsilon_{\mathbf{k}c} + \epsilon_{\mathbf{k}v} + i\eta)(\hbar\omega_L - \epsilon_{\mathbf{k}+Qc'} + \epsilon_{\mathbf{k}+Qv'} - \hbar\omega_{\mathbf{Q}j} - \hbar\omega_{\mathbf{Q}j'} + i\eta)} + \frac{\langle \mathbf{k}v | \partial V / \partial R_{\mu}(\kappa) | \mathbf{k}+Qv' \rangle \langle \mathbf{k}+Qc' | \partial V / \partial R_{\nu}(\kappa') | \mathbf{k}c \rangle}{(\hbar\omega_L + \epsilon_{\mathbf{k}v} - \epsilon_{\mathbf{k}+Qc'} + \hbar\omega_{\mathbf{Q}j} + i\eta)(\hbar\omega_L - \epsilon_{\mathbf{k}c} + \epsilon_{\mathbf{k}v} + i\eta)(\hbar\omega_L - \epsilon_{\mathbf{k}+Qc'} + \epsilon_{\mathbf{k}+Qv'} - \hbar\omega_{\mathbf{Q}j} - \hbar\omega_{\mathbf{Q}j'} + i\eta)} - \left[ \frac{\hbar e_{\mu}^*(\mathbf{Q}, j, \kappa) e_{\nu}(\mathbf{Q}, j', \kappa)}{4M_{\kappa} \omega_{\mathbf{Q}j}^{1/2} \omega_{\mathbf{Q}j'}^{1/2}} + \frac{\hbar e_{\mu}^*(\mathbf{Q}, j, \kappa') e_{\nu}(\mathbf{Q}, j', \kappa')}{4M_{\kappa'} \omega_{\mathbf{Q}j}^{1/2} \omega_{\mathbf{Q}j'}^{1/2}} \right] \right] \quad (2.5c)$$

$$\times \left[ \frac{\langle \mathbf{k}v | \partial V / \partial R_\mu(\kappa) | \mathbf{k}v' \rangle \langle \mathbf{k}c' | \partial V / \partial R_\nu(\kappa') | \mathbf{k}c \rangle}{(\hbar\omega_L + \epsilon_{\mathbf{k}v'} - \epsilon_{\mathbf{k}c} + i\eta)(\hbar\omega_L - \epsilon_{\mathbf{k}c} + \epsilon_{\mathbf{k}v} + i\eta)(\hbar\omega_L - \epsilon_{\mathbf{k}c'} + \epsilon_{\mathbf{k}v'} + i\eta)} + \frac{\langle \mathbf{k}v | \partial V / \partial R_\mu(\kappa) | \mathbf{k}v' \rangle \langle \mathbf{k}c' | \partial V / \partial R_\nu(\kappa') | \mathbf{k}c \rangle}{(\hbar\omega_L + \epsilon_{\mathbf{k}v} - \epsilon_{\mathbf{k}c'} + i\eta)(\hbar\omega_L - \epsilon_{\mathbf{k}c} + \epsilon_{\mathbf{k}v} + i\eta)(\hbar\omega_L - \epsilon_{\mathbf{k}c'} + \epsilon_{\mathbf{k}v'} + i\eta)} \right] \quad (2.5c)$$

which corresponds to the electron and hole each emitting a phonon, and

$$\chi_{\alpha\beta}(\mathbf{k}v, \mathbf{k}c, \mathbf{k}'v', \mathbf{k}'c') = \frac{e^2 \hbar^2}{m^2 V_0} \frac{\langle \mathbf{k}'v' | p_\alpha | \mathbf{k}'c' \rangle \langle \mathbf{k}c | p_\beta | \mathbf{k}v \rangle}{\epsilon_{\mathbf{k}'c'} - \epsilon_{\mathbf{k}'v'} \quad \epsilon_{\mathbf{k}c} - \epsilon_{\mathbf{k}v}} \quad (2.5d)$$

is the electronic susceptibility. Here,  $M_\kappa$  is the mass of atom  $\kappa$  in the basis,  $e_\mu(\mathbf{Q}, j, \kappa)$  is the  $\mu$ th component of a phonon polarization vector,  $R_\mu(\kappa)$  is the coordinate of atom  $\kappa$  of the basis with respect to a chosen zero,  $\tau_\kappa$  is the coordinate of atom  $\kappa$  with respect to the center of the bond between the two basis atoms,  $p_\alpha$  are the components of the momentum operator,  $e$  is the electron's charge and  $m$  its free mass, and  $V_0$  is the volume of a primitive cell.

To simplify the calculation, the self-energies of the electrons, holes, and phonons have not been included. As discussed in the next section,  $\eta$  is treated as a small fixed parameter to produce Lorentzian broadening.

In deriving (2.5), the condition of translational invariance has been used to rewrite the matrix elements of the second-order electron-phonon interaction in terms of products of matrix elements of the first-order electron-phonon interaction.<sup>20</sup> This allows one to combine diagrams 1(a) and 1(c), and 1(b) and 1(d) into two diagrams each with a renormalized electron-two-phonon vertex such as given in (2.5b).

In addition to the two Bose factors in (2.2), weak-temperature dependence also enters from band-gap renormalization<sup>20</sup> and the temperature dependence of the phonon energies, but is neglected here. Experimentally, the product of Bose factors accurately accounts for the temperature dependence,<sup>21</sup> except near resonance.<sup>22</sup> Excitonic effects may be neglected in Si, the material to which the theory will be applied, due to its large static dielectric constant.<sup>23</sup> Only deformation-potential electron-phonon interactions are considered since in Si there are neither piezoelectric nor Fröhlich couplings.

In order to make a quantitative comparison with experimental data (which are usually measured in arbitrary units), the 12 diagrams [isomorphic to Figs. 1(a) and 1(b) with the electron-two-phonon vertex replaced by an electron-one-phonon vertex] contributing to the first-order Raman tensor  $a_{yz}^{(1)}(j)$  were also evaluated, and the normalized scattering tensor

$$\frac{I_{\alpha\beta\gamma\delta}^{(2)}(\omega_R)}{\int_j \sum |a_{yz}^{(1)}(j)|^2 [n(\omega_{0j}) + 1] \delta(\omega_R - \omega_{0j}) d\omega_R} \equiv \frac{I_{\alpha\beta\gamma\delta}^{(2)}(\omega_R)}{(a_{yz}^{(1)})^2} \quad (2.6)$$

plotted. Experimental data measured in arbitrary units can be similarly normalized and thus quantitatively compared with theory.

### III. NUMERICAL PROCEDURE

In this section we discuss the evaluation of the expressions obtained in Sec. II for application to crystalline silicon under no and under [001] stress.

The electronic structure was obtained from local empirical pseudopotentials with a basis of 89 plane waves. Spin-orbit splitting in Si cannot be resolved and thus is not included in the calculation. The pseudopotential form factors  $V(Q)$  for  $\mathbf{Q}$  equal to reciprocal-lattice vectors were obtained from Cohen and Bergstresser.<sup>24</sup> In the evaluation of the electron-phonon matrix elements, the rigid-pseudoion model was employed; that is, each atom was assumed to have a local pseudopotential which rigidly moves with the atom as it is displaced by the phonon. In order to evaluate the electron-phonon matrix elements  $V(Q)$  is needed for arbitrary value of  $Q$ . Thus a smooth interpolation was performed between the Cohen and Bergstresser values, with an upper cutoff at  $Q^2 = 12(2\pi/a)^2$ , where  $a$  is the lattice spacing, and a lower limit of  $V(0) = -\frac{2}{3}E_F$ , where  $E_F$  is the Fermi energy of an electron gas of the same density as the valence electrons. As shown in Ref. 10, this choice of  $V(0)$  gives spectra which differ slightly from those obtained from the choice  $V(0) = 0$ .<sup>25</sup> For a discussion concerning appropriate interpolations and screenings of pseudopotential form factors, see Ref. 20.

Phonon frequencies and eigenvectors were obtained using Weber's bond-charge model parametrization.<sup>26</sup> Experimental determination of certain phonon eigenfrequencies and eigenvectors indicates that the bond-charge model is among the best phonon models for Si.<sup>27</sup>

A Lorentzian broadening of  $\eta = 0.1$  eV is used throughout the calculation in order to take into account the lifetime broadening of the electronic states as well as to smooth out fluctuations arising from the finite mesh size employed in the Brillouin-zone integrations. The results are insensitive to the exact choice of this parameter. For the case of an unstressed tetrahedral semiconductor, the  $\mathbf{Q}$  summation was performed over 28 points in an irreducible 1/48 wedge in the Brillouin zone employing the tetrahedron method.<sup>28</sup> The  $\mathbf{k}$  summation was performed over 480 special points<sup>29</sup> in the entire Brillouin zone.

The effects of uniaxial stress on the electronic structure are taken into account through the multiplication of all real-space vectors by  $1 - \epsilon_{\alpha\beta}$ , where  $\epsilon_{\alpha\beta}$  is the strain tensor, and the multiplication of all reciprocal-lattice vectors by  $1 - \epsilon_{\alpha\beta} \approx (1 + \epsilon_{\alpha\beta})^{-1}$ . This treatment is exact for [001]

stress; for [111] stress in addition a sublattice shift determined the internal strain parameter<sup>30</sup> would have to be included. Under [001] stress, the point group of the crystal is reduced from  $O_h$  to  $D_{4h}$ , requiring that the  $\mathbf{Q}$  sum be performed over an irreducible  $\frac{1}{16}$  portion of the Brillouin zone. For this stress,  $\epsilon_{\alpha\beta}$  is diagonal with elements  $\epsilon_{xx} = \epsilon_{yy} = XS_{12}$ , and  $\epsilon_{zz} = XS_{11}$  where  $X$  is the stress and  $S_{ij}$  are the elastic compliance constants. We take  $S_{11} = 7.68 \times 10^{-13}$  cm<sup>2</sup>/dyn and  $S_{12} = -2.14 \times 10^{-13}$  cm<sup>2</sup>/dyn.<sup>31</sup> The weak stress dependence of the phonon dispersion has been neglected.

A typical calculation of all the independent components of the scattering tensor required  $\sim 42$  h CPU time on a Comparex 242. This time can be reduced significantly by increasing the mesh spacing of the Brillouin-zone sums, but only at the price of introducing more numerical noise.

#### IV. RESULTS AND DISCUSSION

In this section results of the evaluation of (2.6) are compared with experimental data for crystalline silicon<sup>14</sup>

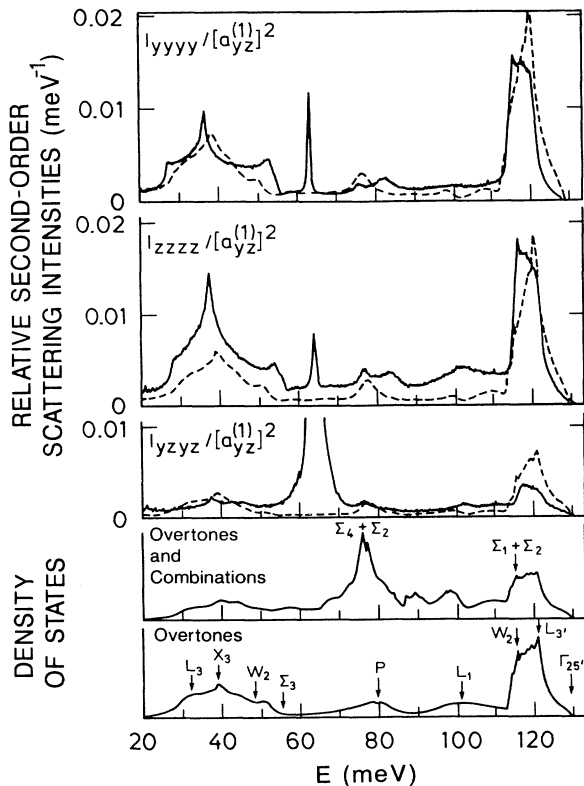


FIG. 2. Calculated (dashed) and experimental (solid) relative second-order scattering intensities of Si in the absence of stress, as a function of the Raman shift  $E = \hbar\omega_R$ . Plotted are the three components corresponding to the three experimental scattering configurations. The incident photon propagates in the  $\hat{x}$  direction and has energy 2.34 eV. Features of the spectra may be compared with van Hove singularities of the combination and overtone phonon density of states shown at the bottom of the figure.

obtained at room temperature with a 531-nm laser beam off the [100] surface of the Si sample under various [001] stresses up to 24 kbar. Rather than calculating the three (for no stress) irreducible components of the second-order spectra ( $\Gamma_1, \Gamma_{12}$ , and  $\Gamma_{25'}$ ), the measured components  $I_{yyyy}^{(2)}$  [corresponding to scattering configuration  $x(yy)\bar{x}$ : incident photon propagates in the  $x$  direction and is polarized along  $y$ , and the scattered photon propagates in the  $-x$  direction and is also polarized along  $y$ ],  $I_{zzzz}^{(2)}$  [scattering configuration  $x(zz)\bar{x}$ ] and  $I_{yzyz}^{(2)}$  [scattering configuration  $x(yz)\bar{x}$ ] were directly calculated. In the absence of stress,  $I_{yyyy}^{(2)} = I_{zzzz}^{(2)} = I_{\Gamma_1} + 4I_{\Gamma_{12}}$  and  $I_{yzyz}^{(2)} = I_{\Gamma_{25'}}$ .

A comparison between the calculation (dashed line) and the experimental (solid line) data for unstressed Si is shown in Fig. 2, where both theoretical and experimental data have been normalized as in (2.6). Also plotted are the overtone and combination phonon density of states obtained from the bond-charge model. As is typical of tetrahedral semiconductors,  $I_{yyyy}^{(2)}$  and  $I_{zzzz}^{(2)}$  are roughly proportional to the phonon overtone density of states. This is not the case for alkali halides,<sup>8</sup> for example. Figure 2 shows good agreement between the calculated and experimental spectra for all three components (similar to those reported in Ref. 10); the magnitudes and the normalized scattering efficiencies match well. In Fig. 2, first-order scattering is only allowed in the  $x(yz)\bar{x}$

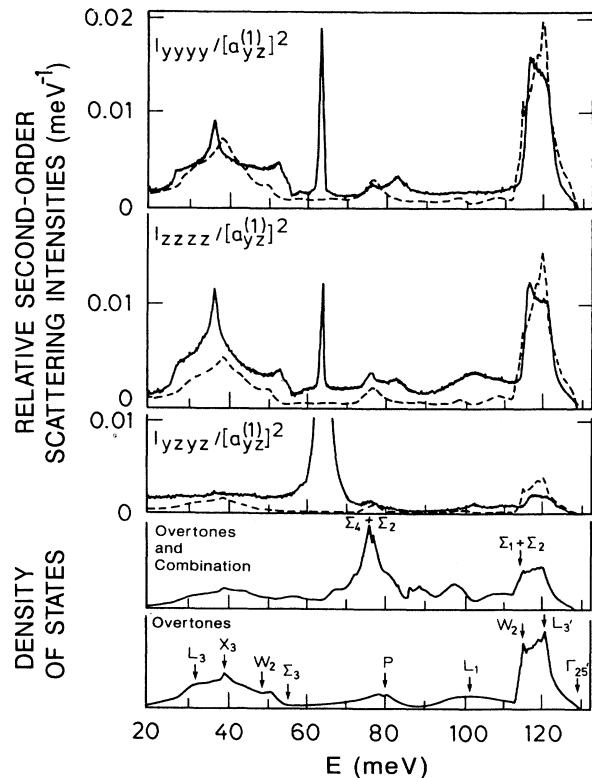


FIG. 3. Same as Fig. 2 except the sample is now under 24 kbar [001] stress.



icates that for the TA phonons at  $X$  with photon polarizations along the stress axes and parallel to each other ( $I_{zzzz}$ ) one should observe mainly the  $X_{001}$ . For photons polarized perpendicular to the stress and parallel to each other ( $I_{xxxx}$  and  $I_{yyyy}$ ) one observes mainly  $X_{100}$  and  $X_{010}$ . The difference, however, is not large and if the splitting by stress is to be ascertained from the piezoelectric Raman results, a careful fit to the experimental data with the weights given by the calculation of Fig. 6 is needed. The strain-induced conduction-band intervalley splitting usually shifts the  $Q\|\hat{z}$  component down and raises the other two components, relative to the intrinsic splittings of Fig. 4. In general, the electronic or phonon-energy shift due to a strain given by the tensor  $\bar{\epsilon}$  is<sup>32</sup>

$$\Delta E = (D_1 \bar{1} + D_2 \{\hat{\mathbf{a}}\hat{\mathbf{a}}\}) : \bar{\epsilon}, \quad (4.1)$$

where  $\hat{\mathbf{a}}$  is a unit vector in the direction of the wave vector of the electron or phonon,  $\bar{1}$  is the unit tensor,  $\{\}$  denotes a dyadic product, and  $D_1$  and  $D_2$  are constants. Thus the  $L$  phonons will remain unsplit under [001] stress, while the  $W$  points will split.

As an example of employing the weights of Figs. 4 and 6, we calculate some of the generalized mode Grüneisen parameters of Si, employing also the experimental piezoelectric Raman data. The generalized mode Grüneisen parameters  $\gamma_{kl}(\mathbf{Q}, j, m)$  for a branch  $j$  phonon polarized

along  $m$  (if transverse) with wave vector  $\mathbf{Q}$  are defined in terms of the frequency-shift squared  $\Delta\omega^2(\mathbf{Q}, j, m)$  induced by strain  $\epsilon_{kl}$  to the unstrained frequency  $\omega_0^2(\mathbf{Q}, j)$  as<sup>33</sup>

$$\Delta\omega^2(\mathbf{Q}, j, m) = -2\omega_0^2(\mathbf{Q}, j) \sum_{kl} \gamma_{kl}(\mathbf{Q}, j, m) \epsilon_{kl}(\sigma), \quad (4.2)$$

where  $\sigma$  is the magnitude of the stress, taken to be negative for a compressive stress. Thus, for TA( $X$ ) phonons under [001] stress and for small frequency shifts  $\Delta\omega$ , the  $\Delta\omega$  are given by

$$\Delta\omega = -\omega_0 \sigma (S_{11} \gamma_{11} + 2S_{12} \gamma_{22}) \quad \text{for } \mathbf{Q}\|\text{stress} \quad (4.3a)$$

and

$$\Delta\omega = -\omega_0 \sigma [S_{11} \gamma_{22} + S_{12} (\gamma_{11} + \gamma_{22})] \quad \text{for } \mathbf{Q}\perp\text{stress}. \quad (4.3b)$$

Since the "intervalley" splitting of TA( $X$ ) phonons, to be

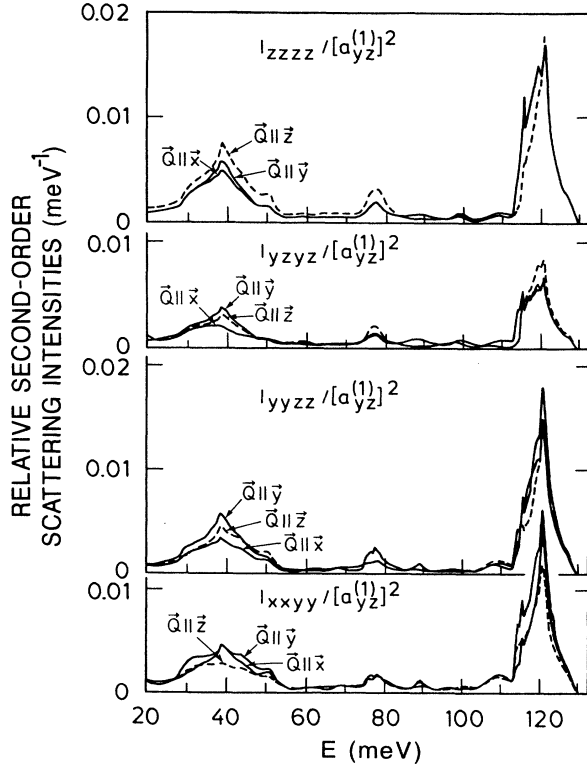


FIG. 6. Same as Fig. 4 except the sample is under 24 kbar [001] stress; this gives the added contributions of the stress-induced intervalley splitting.

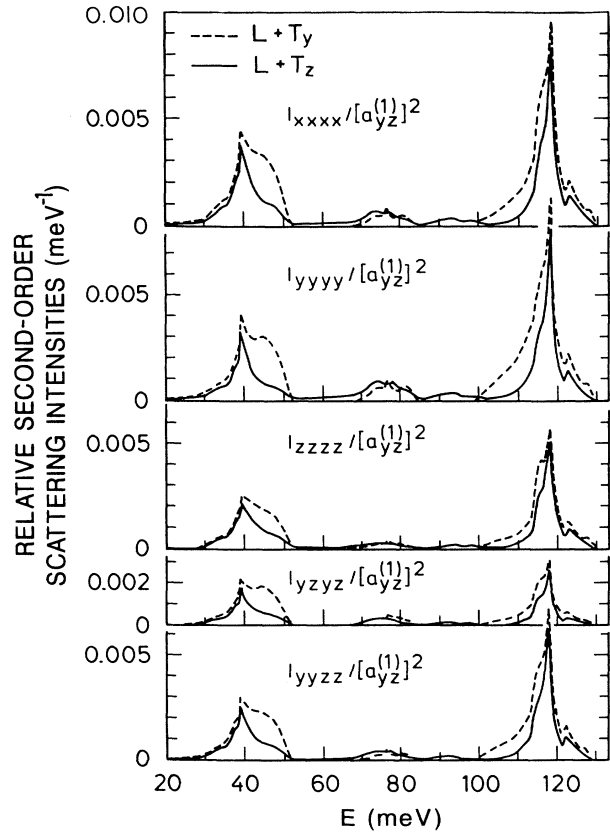


FIG. 7. Calculated spectra with sample under 24 kbar [001] stress and the two contributions of the transverse-phonon polarizations separated in order to display intravalley splitting. The dashed line gives the contributions of all longitudinal phonons and those transverse phonons polarized perpendicular to the stress, and the solid line gives the contributions of all longitudinal phonons and those transverse phonons polarized parallel to the stress. The phonon  $\mathbf{Q}$  vector has been restricted to be approximately parallel to the  $\hat{\mathbf{x}}$  axis.

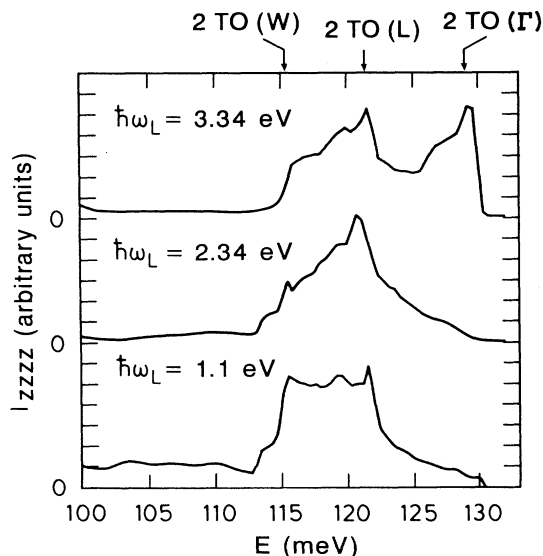


FIG. 8. Calculated second-order Raman spectra of Si showing the  $I_{zzzz}$  component in the absence of stress for three different laser frequencies. The relative amplitudes of the  $2TO(W)$ ,  $2TO(L)$  and  $2TO(\Gamma)$  peaks vary with laser frequency as different intermediate states become resonant.

discussed next, cannot be resolved in the experimental data, we neglect the contributions of  $\gamma_{23}$  which determines the magnitude of the splitting. The experimental data indicate that the  $2TA(X)$  peak in the  $I_{yyyy}$  spectrum occurs at  $301.48 \text{ cm}^{-1}$  under no stress, and at  $300.18 \text{ cm}^{-1}$  under 24 kbar [001] stress. Also, this peak falls in the  $I_{zzzz}$  spectrum at  $301.48 \text{ cm}^{-1}$  under no stress, and at  $298.77 \text{ cm}^{-1}$  under stress. The resolution on the energy scale is  $1.3 \text{ cm}^{-1}$ . The relative weights of  $Q_{\parallel}$  stress and  $Q_{\perp}$  stress can be determined from Figs. 4 and 6. Using these to weight equations (4.3a) and (4.3b), we obtain  $\gamma_{11} = -1.50$  and  $\gamma_{22} = -0.33$  for  $TA(X)$  phonons, and a Grüneisen parameter of  $\gamma_G = (\gamma_{11} + 2\gamma_{22})/3 = -0.72$ . More accurate determinations of these parameters using neutron scattering give  $\gamma_{11} = -2.05 \pm 0.19$  and  $\gamma_{22} = -1.59 \pm 0.24$ ,<sup>33</sup> and  $\gamma_G = -1.74$ . The generally accepted value of  $\gamma_G$  for  $TA(X)$  phonons is  $-1.4$ .<sup>34</sup> It is probable that the low resolution of the Raman data is at fault with the disagreement; however, higher resolution data, combined with the calculated weights, should provide an alternative method for the accurate determination of mode Grüneisen parameters.

Besides the intervalley splitting of  $X_{001}$  versus  $X_{100}$  and  $X_{010}$ , the strain also induces an intravalley splitting of the directions ("valleys")  $X_{100}$  and  $X_{010}$ . Each of them contains transverse vibrations along and perpendicular to the stress axis, degenerate for zero stress but split by the stress. In Fig. 7 these intravalley splittings are presented. Each curve in the figure includes the contributions of all longitudinal phonons but only one polarization (perpendicular or parallel to the stress) of the transverse pho-

ns, for the case of 24 kbar [001] stress and  $Q_{\parallel}\hat{x}$ . Since it is often impossible to assign phonons to longitudinal or transverse branches away from symmetry points, the results of Fig. 7 do not show a complete separation of the two polarization directions of the transverse phonons, or show equal contributions from the longitudinal branches. In particular, it appears that the  $L + T_y$  (all longitudinal and those transverse phonons polarized along  $y$ ) curve contains the contributions of too many  $T_z$  phonons near  $W$  and thus the calculated difference between the  $L + T_y$  and  $L + T_z$  spectra near  $W$  is too large. Nevertheless, the calculations should help to provide an estimate of the intravalley splittings near  $X$  and  $L$ .

By inspection of the calculated Raman tensor for various  $Q$  values, one can establish that resonant intermediate states dominate the transition amplitude. Resonant intermediate states occur when, for example, the first-energy denominator in (2.5b) becomes zero. The calculations show, in agreement with experiment,<sup>35</sup> that the relative heights of the  $2TO(W)$ ,  $2TO(L)$ , and  $2TO(\Gamma)$  peaks vary with changing incident photon energies (Fig. 8). Above the indirect gap, the  $2TO(W)$  peak dominates, but with increasing  $\hbar\omega_L$  the  $2TO(L)$  peak starts to dominate (at about  $\hbar\omega_L = 2.2 \text{ eV}$ ) as resonant transitions become possible to  $\Lambda$  states. Finally, near the direct gap, the  $TO(\Gamma)$  phonons produce a strongly resonant intermediate state.

## V. CONCLUSION

In summary, we have calculated the second-order Raman-scattering efficiency for semiconductors under uniaxial stress. The theory is valid for light frequencies either on or off resonance. Quantitative comparison with experimental data for crystalline Si both unstressed (Fig. 2) and under [001] stress (Fig. 3) shows good agreement both in the amplitude and the form of the scattering spectrum. The calculation allows one to separate out the contributions of given phonons and phonon polarizations allowing for the determination of intervalley and intravalley splittings in the spectra.

The main source of errors in the numerical evaluation is the large grid spacing employed in the Brillouin-zone sums, which was not reduced because of the already lengthy nature of the calculations. For this reason also, the relaxation of the approximations made or the extension to third- or higher-order scattering would require faster computing capabilities. Nevertheless, these microscopic calculations demonstrate agreement with experiment at a level comparable to that of phenomenological theories.

## ACKNOWLEDGMENTS

The authors wish to thank E. Anastassakis and A. Cantarero for providing the experimental data prior to publication, and C. Trallero-Giner for a critical reading of the manuscript. One of us (C.G.) acknowledges partial support of the Natural Sciences and Engineering Research Council of Canada.

- <sup>1</sup>For a review, see *Light Scattering in Solids*, edited by M. Cardona, Topics of Applied Physics Vol. 8 (Springer-Verlag, Berlin, 1975) and further volumes in this series.
- <sup>2</sup>M. Born and K. Huang, *Dynamical Theory of Crystal Lattices* (Clarendon, Oxford, 1956).
- <sup>3</sup>R. Zeyher, Phys. Rev. B **9**, 4439 (1974).
- <sup>4</sup>R. A. Cowley, Proc. Phys. Soc. **84**, 281 (1964).
- <sup>5</sup>R. Loudon, Adv. Phys. **13**, 423 (1964); Proc. R. Soc. London Ser. A **275**, 218 (1963); J. Phys. **26**, 677 (1965).
- <sup>6</sup>A. Ganguly and J. Birman, Phys. Rev. **162**, 806 (1967).
- <sup>7</sup>A. Kawabata, J. Phys. Soc. Jpn. **30**, 68 (1971).
- <sup>8</sup>A. Pasternak, E. Cohen, and G. Gilat, Phys. Rev. B **9**, 4584 (1974).
- <sup>9</sup>S. Go, H. Bilz, and M. Cardona, Phys. Rev. Lett. **34**, 580 (1975).
- <sup>10</sup>M. Cardona and P. B. Allen, Helv. Phys. Acta **58**, 307 (1985).
- <sup>11</sup>E. Anastassakis, F. Pollak, and G. W. Rubloff, Phys. Rev. B **9**, 551 (1974).
- <sup>12</sup>W. Richter, R. Zeyer, and M. Cardona, Phys. Rev. B **18**, 4312 (1978).
- <sup>13</sup>V. G. Khamdamov, I. I. Novak, and V. I. Vottegren, Fiz. Tverd. Tela (Leningrad) **26**, 327 (1984) [Sov. Phys.—Solid State **26**, 195 (1984)].
- <sup>14</sup>E. Anastassakis and A. Cantarero (private communication).
- <sup>15</sup>T. P. Pearsall, J. M. Vandenberg, R. Hull, and J. M. Bonar, Phys. Rev. Lett. **63**, 2104 (1989).
- <sup>16</sup>R. Zachai, K. Eberl, G. Abstreiter, E. Kasper, and H. Kibbel, Phys. Rev. Lett. **64**, 1055 (1990).
- <sup>17</sup>M. V. Klein, Phys. Rev. B **24**, 4208 (1981).
- <sup>18</sup>M. Cardona, *Light Scattering in Solids II*, edited by M. Cardona and G. Güntherodt (Springer-Verlag, Berlin, 1982).
- <sup>19</sup>G. D. Mahan, *Many-Particle Physics* (Plenum, New York, 1981).
- <sup>20</sup>P. B. Allen and M. Cardona, Phys. Rev. B **27**, 1495 (1981).
- <sup>21</sup>P. A. Temple and C. E. Hataway, Phys. Rev. B **7**, 3685 (1973).
- <sup>22</sup>A. Compaan and H. J. Trodahl, Phys. Rev. B **29**, 793 (1984).
- <sup>23</sup>P. Lautenschlager, M. Garriga, L. Vina, and M. Cardona, Phys. Rev. B **36**, 4821 (1987).
- <sup>24</sup>M. L. Cohen and T. K. Bergstresser, Phys. Rev. **141**, 789 (1960).
- <sup>25</sup>S. Bednarek and U. Rössler, Phys. Rev. Lett. **48**, 1296 (1982).
- <sup>26</sup>W. Weber, Phys. Rev. B **15**, 4789 (1977); O. H. Nielsen and W. Weber, Comput. Phys. Commun. **18**, 101 (1979).
- <sup>27</sup>D. Strauch, A. P. Mayer, and B. Dorner, Z. Phys. B **78**, 405 (1990).
- <sup>28</sup>G. Lehmann and M. Taut, Phys. Status Solidi B **54**, 469 (1972).
- <sup>29</sup>D. J. Chadi and M. L. Cohen, Phys. Rev. B **8**, 5747 (1973); J. Pack, *ibid.* **13**, 5188 (1977).
- <sup>30</sup>L. Kleinman, Phys. Rev. **128**, 2614 (1962).
- <sup>31</sup>*AIP Handbook*, edited by D. E. Gray (McGraw-Hill, New York, 1972).
- <sup>32</sup>W. C. Herring and E. Vogt, Phys. Rev. **101**, 944 (1956).
- <sup>33</sup>J. Prechtel, J. Kalus, E. Lüscher, L. Pintschovius, and R. Ghosh, Phys. Status Solidi B **93**, 653 (1979).
- <sup>34</sup>B. A. Weinstein and R. Zallen, in *Light Scattering in Solids IV*, edited by M. Cardona and G. Güntherodt (Springer-Verlag, Berlin, 1984).
- <sup>35</sup>J. B. Renucci, R. N. Tyte, and M. Cardona, Phys. Rev. B **11**, 3885 (1975).